Research Article | Vol. 14, No. 5 / 1 May 2023 / Biomedical Optics Express 2386

Biomedical Optics EXPRESS

Detection speed optimization of the OI-RD microscope for ultra-high throughput screening

HANG ZHANG,[1] MENGJING XU,[1] HAOFENG LI,[1] XIAOHAN MAI,[1] JIAWEI SUN,[2] LAN MI,[1] JIONG MA,[1] XIANGDONG ZHU,[3] AND YIYAN FEI[1,*]

[1]*Department of Optical Science and Engineering, Shanghai Engineering Research Center of Ultra-Precision Optical Manufacturing, Key Laboratory of Micro and Nano Photonic Structures (Ministry of Education), School of Information Science and Technology, Fudan University, Shanghai, 200433, China*
[2]*Department of Science and Technology, Shanghai Deyu Intelligent Technology Co., Ltd., Shanghai, 201413, China*
[3]*Department of Physics, University of California, One Shields Avenue, Davis, California 95616, USA*
[*]*fyy@fudan.edu.cn*

Abstract: The oblique-incidence reflectivity difference (OI-RD) microscope is a label-free detection system for microarrays that has many successful applications in high throughput drug screening. The increase and optimization of the detection speed of the OI-RD microscope will enable it to be a potential ultra-high throughput screening tool. This work presents a series of optimization methods that can significantly reduce the time to scan an OI-RD image. The wait time for the lock-in amplifier was decreased by the proper selection of the time constant and development of a new electronic amplifier. In addition, the time for the software to acquire data and for translation stage movement was also minimized. As a result, the detection speed of the OI-RD microscope is 10 times faster than before, making the OI-RD microscope suitable for ultra-high throughput screening applications.

1. Introduction

Drug discovery is often characterized by a long research and development process, high investment, and high technology, which aims to identify new drugs. As an important starting point for drug discovery, drug screening aims to look for candidate compounds with the potential to be developed as drugs through high throughput screening (HTS) from libraries including about $10^4 \sim 10^7$ drug-like compounds [1,2]. HTS usually has a capacity to analyze around 10,000 compounds per day. The need to screen millions of compounds for an increasing number of targets has driven the development of ultra-high throughput screening (uHTS), with the potential to analyze up to 100,000 compounds per day [2–4], which is more cost-effective and time-efficient than HTS.

Fluorescence-based optical assays are widely used in the field of HTS due to their advantages of high sensitivity and flexibility. Fluorescence anisotropy/polarization (FA/FP) is a commonly employed technology in HTS [5], which can measure the interactions between labeled molecules and targeted proteins, and have found applications in the discovery of anti-inflammatory agent INCA-6 [6], inhibitors of FtsZ-ZipA [7], WDR5-MLL1 [8], and EZH2-EED [9]. The FA/FP based uHTS platform has been developed and employed in measuring the activity of an adenine transferase and identifying the inhibitors of FEN1 [10,11]. Time-resolved fluorescent resonance energy transfer (TR-FRET) is another versatile technology with a variety of biochemical applications in HTS, including discovery of small molecule modulators of the actin-myosin interaction and inhibitors of methyl-lysine reader proteins [12,13]. The TR-FRET based uHTS platform has been used to identify the inhibitors of 14-3-3 protein and a compound disrupting the NSD3-MYC interaction [14,15]. Many fluorescence-based assays, including FA/FP and

#487563 https://doi.org/10.1364/BOE.487563
Journal © 2023 Received 14 Feb 2023; revised 18 Apr 2023; accepted 19 Apr 2023; published 28 Apr 2023

Biomedical Optics EXPRESS

TR-FRET technologies, take advantages of microplates for HTS and uHTS [16–18]. In addition to the microplate-based assays, microarrays are also used in HTS through the immobilization of tens of thousands of compounds on a single glass slide to form small molecule microarrays (SMMs), which are usually detected by fluorescence-based methods and have found applications in the discovery of EWS-FLI modulator [19], histone deacetylase inhibitors [20], and Aurora A ligand [21]. Even though fluorescence-based detection technologies have been widely used in both HTS and uHTS, the disadvantages, including inaccurate measurements caused by labeled biomolecules [22,23], costly, and laborious labeling processes, are unavoidable so that label-free based screening technologies are desirable to minimize problems associated with labels.

A novel high-throughput screening platform based on SMMs and oblique-incidence reflectivity difference (OI-RD) microscope has been developed to look for small molecules binding to target proteins through label-free measurement of surface mass density change of molecules immobilized on surface [24–28]. Label-free detection of biomolecular interactions by OI-RD gets rid of labeling effects of biomolecules and minimizes false positives due to labeling effects. SMMs and OI-RD microscope have been widely applied in HTS and have successfully found the autophagosome-tethering compound (ATTEC) for mutant HTT protein [29] and inhibitors for different target proteins [30–34]. OI-RD has the capability to screen around 20,000 samples per day, which demonstrates the potential as an alternative and powerful technology for HTS. Further development of OI-RD for uHTS will enable its wider applications in industry of drug screening.

This work presents the increase and optimization of detection speed of OI-RD microscope by minimizing the wait time for lock-in amplifier, the time for software to acquire data, and the time for translation stage movement. After optimization, the time to scan an OI-RD image was reduced from ~ 104 min to ~ 12 min, so that the screening throughput can be increased from 20,000 samples to around 200,000 samples per day, making OI-RD microscope suitable for uHTS.

2. Methods

2.1. Detection process and time spent on each step of scanning an OI-RD image

Figure 1(a) shows that OI-RD detects a microarray by laser (HÜBNER Photonics, Cobolt08) scanning along vertical direction and translation stage (Physik Instrumente, M505) scanning along horizontal direction [24,25], which gives an OI-RD image of the microarray. At the beginning of the scanning process, laser light is incident at the upper right corner of the microarray. The laser light scans from top to bottom of the microarray by clockwise rotation of the galvanometer (Cambridge Technology, 6M2210R44B050S4) for 780 steps, with optical signal of each step being detected and converted into voltage signal by a linear photodiode. The voltage signal is then amplified by a custom-designed and fabricated electronic amplifier (Home-made, Fig. S3 within the Supplement 1). Since OI-RD signal is modulated by a photo-elastic modulator (PEM, HINDS Instruments, PEM-100) at frequency of 50 kHz, the amplified signal is detected by a lock-in amplifier (LIA, Zurich Instruments, MFLI DEV5307) which is able to detect and measure very small AC signals even when the small signal is obscured by noise sources many thousands of times larger [35,36]. After vertical scanning of the laser light, the galvanometer quickly returns back to the top and the translation stage housing the flow cell with microarray moves one step toward right along the horizontal direction. The inner loop of Fig. 1(b) shows that the time for each step of laser scanning from top to bottom includes the wait time (3 ms) for LIA and software time (~ 0.78 ms) to acquire data. The outer loop in Fig. 1(b) shows that the time for the translation stage movement includes elapsed time before stage movement (50 ms) and elapsed time after stage movement (150 ms) which covers the stage movement time (~ 11.09 ms) due to their synchronous timing. Long enough elapsed time is used to guarantee that both galvanometer and translation stage don't move when software acquires data. With 1980 steps of the translation stage movement along the horizontal direction, the total scanning time of an OI-RD image is ~ 104 min (Table 1) which can be roughly divided into three parts, (1) the wait time for LIA is

Biomedical Optics EXPRESS

about 77 min, which is roughly 74% of the total time; (2) the time for software to acquire data is about 20 min, which is roughly 19% of the total time; (3) the time for translation stage movement is about 7 min, which is roughly 7% of the total time.

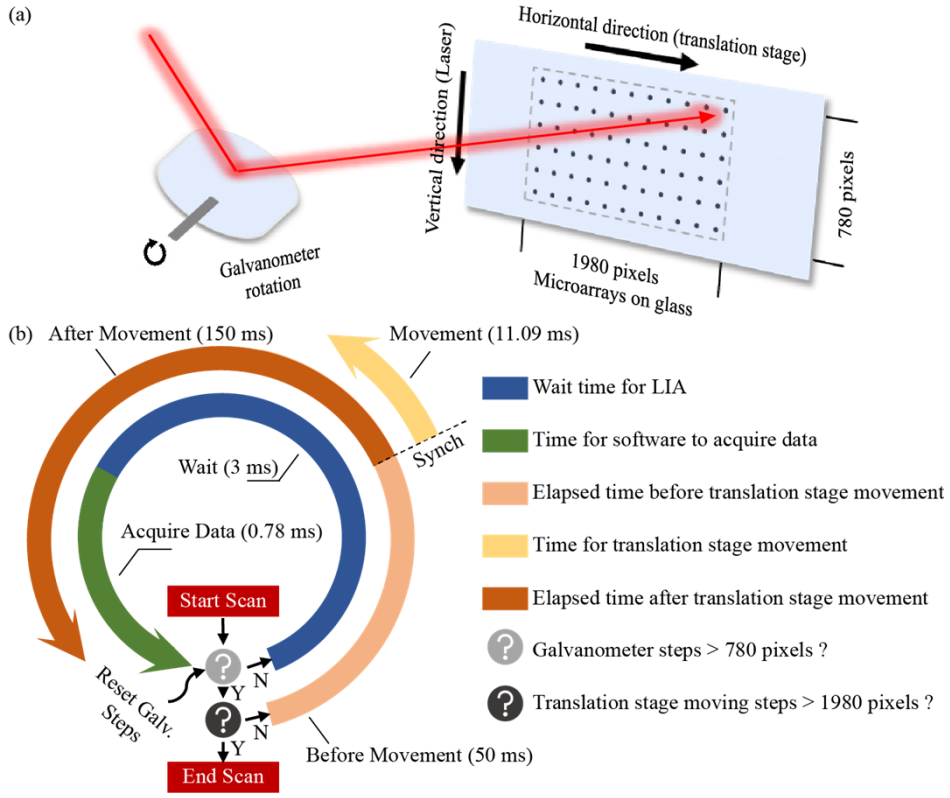

Fig. 1. (a) Detection process and (b) time spent on each step of scanning an OI-RD image

Table 1. Time spent on each step of scanning an OI-RD image before speed optimization

	Time (min)	Percentage (%)	Time calculation (ms)
Total wait time for LIA	~ 77	~ 74	1980 × 780 × 3
Total software time to acquire data	~ 20	~ 19	1980 × 780 × 0.78
Total translation stage movement time	~ 7	~ 7	1980 ×200
Total time of scanning an OI-RD image	~ 104	100	

2.2. *Basic information of input and output for a LIA*

To reduce the detection time of an OI-RD image and to optimize the detection speed of OI-RD microscope, the most important step is to minimize the wait time for LIA which takes up about 74% of the detection time for an OI-RD image, as shown in Table 1. Before optimization, the wait time for LIA is 3 ms, which is 10 times of the time constant at 0.3 ms of LIA for the reason that LIA needs time to reach final values. The wait time for LIA varies with both time constant and the slope of the low-pass filter (LPF) inside LIA. According to the manual of LIA, the wait time should be at least 4.6 times of time constant with a slope of 6 dB/oct, 6.6 times of time

Biomedical Optics EXPRESS

constant with a slope of 12 dB/oct, 8.4 times of time constant with a slope of 8 dB/oct, and 10 times of time constant with a slope of 24 dB/oct, respectively. To minimize the wait time, one feasible way is to reduce LPF slope or time constant. However, reducing the wait time for LIA by decreasing the slope or time constant inevitably increases the noises of OI-RD signals, thus degrades OI-RD image quality. To reduce the wait time, it is necessary to analyze noise sources and find ways to minimize noise levels while reducing wait time.

OI-RD noise mainly comes from three sources. One source of noise is associated with the electronic amplifier, and typically has contributions by various factors such as internal electronic noise, fluctuations in light sources, and environmental disturbances. OI-RD noise also includes the floor noise (white noise) characterized by a "white" frequency spectrum. Direct current (DC) noise and $1/f$ noise with a noise power inversely proportional to frequency [37,38], which are also present in OI-RD signal. To fully understand impacts of the latter two noises, Fig. 2(a) shows the frequency spectrum of the input signal for LIA which consists of OI-RD signal at modulation frequency f_0, DC noise, $1/f$ noise, and floor noise. LIA amplifies the input signal and then multiplies it by a reference signal with reference frequency being equal to the modulation frequency f_0. After multiplication, the frequency spectrum consists of DC component (difference frequency of OI-RD signal at frequency f_0 with LIA reference signal), signal at f_0 (sum frequency of DC noise and $1/f$ noise with LIA reference signal), and signal at $2f_0$ (sum frequency of OI-RD signal at frequency f_0 with LIA reference signal) (Fig. 2(b)). LPF is then applied to get rid of AC components and DC signal passes LPF for further amplitude measurement (Fig. 2(c)). The attenuation effect of each LPF can be characterized by gain-magnitude function $g(f)$, which is inversely proportional to the frequency f so that not only DC signal but also AC components in Fig. 2(b) with relatively large value of $g(f)$ can pass LPF. Decrease of time constant and LPF slope widens $g(f)$ and more floor noise pass LPF which increases noise level in the LIA output signal. In addition, widened $g(f)$ may not sufficiently attenuated noise at modulation frequency of f_0 in Fig. 2(b) (DC noise and $1/f$ noise in Fig. 2(a)) so that noise level is further increased. To get rid of noise due to under-attenuated DC noise and $1/f$ noise, it is important to determine a critical frequency f_{criti} beyond which LPF reduces DC and $1/f$ noise to negligible level. Modulation frequency f_0 larger than critical frequency f_{criti} should be used which is expected to give signal measurement with negligible contribution from DC and $1/f$ noise.

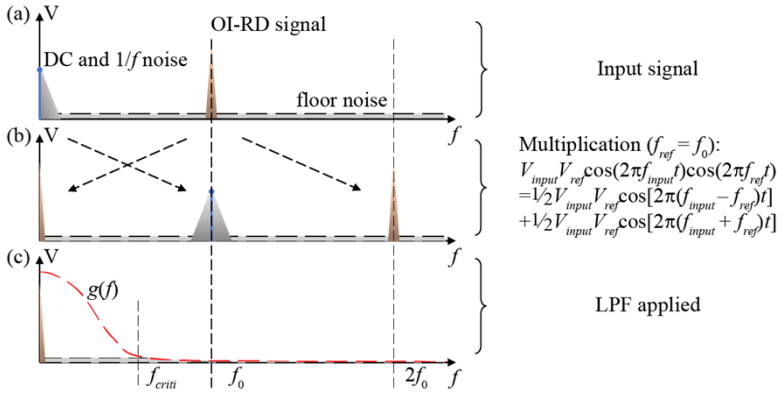

Fig. 2. Schematic diagram of (a) input signal for LIA, (b) signal after multiplication of LIA, (c) and signal after LPF of LIA in frequency domain.

Biomedical Optics EXPRESS

3. Results and discussion

3.1. Dependency of critical frequency f_{criti} on time constant and LPF slope

For effective determination of critical frequency f_{criti}, LIA was not connected with any input (no-load condition) so that LIA only measure noises (including DC noise, 1/f noise, and white noise), which is helpful to understand the dependency of critical frequency f_{criti} on time constant and LPF slope. Based on the analysis of a LIA response to white noise by Van Baak *et al.* [39], this work analyzed LIA response to white noise, DC noise, and 1/f noise. Detailed information of following derivation is included in the Supplement 1. The reference signal $R(t)$ of the LIA is:

$$R(t) = R_r \cos(2\pi f_0 t - \phi_r) \tag{1}$$

where R_r, f_0, and ϕ_r are the amplitude, frequency, and phase of the reference signal, respectively. Here, the frequency of the reference signal is equal to the modulation frequency f_0 of OI-RD microscope.

The no-load noise $U(t)$ can be represented as a discrete Fourier series over duration T:

$$U(t) = \sum_{j=0}^{N} A_j \cos(2\pi j f_1 t - \varphi_j) \tag{2}$$

where the fundamental frequency is $f_1 = 1/T$, and the harmonic frequencies are $f_j = jf_1$ (j is integer). A_j and φ_j are amplitude and phase for the j th frequency, respectively.

The noise variance δV_{out}^2 of LIA output signal can be expressed as:

$$\delta V_{out}^2 = \left(\frac{GR_r A_{WH}}{2V_m}\right)^2 \frac{1}{2\delta f k_n \tau} + \left(\frac{GR_r}{2V_m}\right)^2 g_n^2(f_0)\left[A_{DC}^2 + \sum_{j=1}^{[f_{cn}/f_1]} A_{1/f}^2(jf_1)\right] \tag{3}$$

where V_m is a scale factor of LIA multiplier, G is a linear gain factor applied to signals and noises, τ is the time constant of LIA, k_n is a numerical coefficient varying with the LPF slope, δf is the spectral resolution. A_{WH}, A_{DC}, and $A_{1/f}$ are amplitudes for white noise, DC noise, and 1/f noise, respectively. Particularly, $A_{1/f}$ is inversely proportional to the frequency which can be expressed as $A_{1/f} = \sqrt{K/f}$ with coefficient K. f_{cn} is the corner frequency beyond which the dominated noise switches from 1/f noise to white noise. Besides, $g_n(f)$ represents the gain-magnitude function of the LPF with an n^{th} order slope, whereas $g_n(f_0)$ corresponds to the value of $g_n(f)$ at a specific modulation frequency f_0. The mathematical expression for $g_n(f)$ is as follows:

$$g_n(f) = \sqrt{\frac{1}{[1 + (2\pi\tau f)^2]^n}} \tag{4}$$

where n is the number of LPF inside the LIA with n of 1, 2, 3, 4 corresponding to LPF slope of 6 dB/oct, 12 dB/oct, 18 dB/oct, and 24 dB/oct, respectively.

First term of Eq. (3) is the variance of white noise being the sum of scaled white noise by $g_n(f)$ at each frequency f over the whole spectrum range, which leads to white noise dependence on both time constant τ and LPF slope described by Eq. (4). Second term of Eq. (3) is variance of DC and 1/f noise which is multiplied by value of $g_n(f)$ at modulation frequency of f_0. To determine critical frequency f_{criti}, the ratio of variance of DC and 1/f noise to that of white noise

Biomedical Optics EXPRESS

was defined as R:

$$R = \frac{g_n^2(f_0)\left[A_{DC}^2 + \sum_{j=1}^{[f_{cn}/f_1]} \frac{K}{jf_1}\right]}{A_{WH}^2 / 2\delta f k_n \tau} \tag{5}$$

Critical frequency f_{criti} is the frequency beyond which the contribution of DC and $1/f$ noise to total noise variance δV_{out}^2 is negligible. In this case, the ratio of DC and $1/f$ noise variance to white noise variance R should be small. When time constant τ and LPF slope don't change, the white noise variance doesn't change while the variance of DC and $1/f$ noise becomes smaller with increasing modulation frequency f_0. For the selected time constant τ and LPF slope there must be a critical frequency f_{criti} beyond which R is small. When the time constant τ and LPF slope change, variance of white noise also changes so that there should be different f_{criti} for different time constant τ and LPF slope.

Beyond critical frequency f_{criti} (*i.e.,* modulation frequency f_0 larger than critical frequency f_{criti}), LIA noise is dominated by white noise, whose noise variance being inversely proportional to time constant τ, meaning that 10-fold decrease in time constant τ leads to a factor of 10 increase in noise variance δV_{out}^2. However, such 10-fold relationship doesn't apply when modulation frequency f_0 smaller than critical frequency f_{criti}. Thus, the critical frequency f_{criti} can be determined by finding the turning point of 10-fold relationship between time consent τ and noise variance δV_{out}^2.

Figure 3(a) shows noise variance δV_{out}^2 dependency on modulation frequency f_0 with a LPF slope of 24 dB/oct. The time constants τ of the three curves are 30, 300, and 3000 µs. All three curves show that large variance δV_{out}^2 decreases rapidly with frequency and gradually becomes flat at large modulation frequency f_0. Large variance δV_{out}^2 at small modulation frequency f_0 is mainly due to DC and $1/f$ noise for the reason that $g_n(f_0)$ is too large to be neglected. With increasing modulation frequency f_0, $g_n(f_0)$ decreases rapidly and becomes negligible after critical frequency f_{criti} beyond which 10-fold relationship applies. To clearly demonstrate the 10-fold relationship, the three curves were normalized by the bottom one with time constant τ at 3000 µs. Figure 3(b) shows the three normalized curves from which the critical frequency f_{criti} was determined as ~ 3 kHz with time constant $\tau = 300$ µs and ~ 25 kHz with time constant $\tau = 30$ µs.

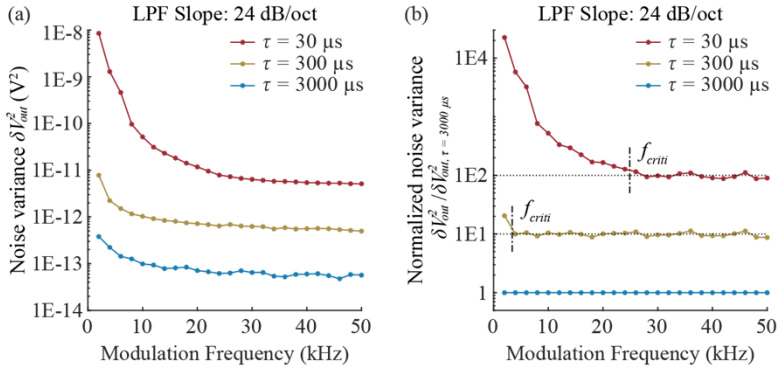

Fig. 3. Relationship of (a) noise variance δV_{out}^2 and (b) normalized noise variance with modulation frequency f_0 measured with LPF slope of 24 dB/oct and three time constants.

Biomedical Optics EXPRESS

The general relationship derived from Eq. (5) between the value of function $g_n(f)$ at f_{criti} with time constant τ and LPF slope is:

$$g_n^2(f_{criti}) = \frac{A_{WH}^2 R}{2(A_{DC}^2 \delta f + K \ln 10^{38}) k_n \tau} \tag{6}$$

where values of A_{WH}, A_{DC} and K were determined by fitting LIA noise spectrum (Fig. S1 within the Supplement 1) under no-load condition with a spectral resolution $\delta f = 5.59 \times 10^{-2}$ Hz. By substituting these values and the two critical frequencies f_{criti} into Eq. (5), R was calculated to be 1/1350. Value of g_n can then be calculated from Eq. (6) for each combination of time constant τ and LPF slope, as listed in Table 2. Based on each value of g_n, critical frequency f_{criti} was then calculated from Eq. (4) (Table 2), which was further verified by experiments (Fig. S2 within the Supplement 1).

Table 2. The $g_n(f_{criti})$ and f_{criti} at different time constant τ and LPF slope

	$g_n(f_{criti})$ (%)				f_{criti} (kHz)			
τ \ slope	6 dB/oct	12 dB/oct	18 dB/oct	24 dB/oct	6 dB/oct	12 dB/oct	18 dB/oct	24 dB/oct
10 µs	0.58	0.41	0.36	0.33	2729.62	247.36	102.91	64.68
30 µs	0.34	0.24	0.21	0.19	1575.96	108.61	**41.35**	**24.91**
100 µs	0.18	0.13	0.11	0.10	863.19	**44.05**	**15.20**	**8.74**
300 µs	0.11	0.08	0.07	0.06	498.37	**19.33**	**6.10**	**3.36**

Since critical frequency f_{criti} listed in Table 2 was determined under conditions with noise only, critical frequency f_{criti} was further verified with input signal generated by a signal generator (RIGOL Technologies, DG1022Z). Figure 4 shows the changes of normalized variance with modulation frequency f_0 with LPF slope of 24 dB/oct and the amplitude of AC signal being 0.1 mV, 1 mV, and 10 mV. Normalized variance curves show that previously determined critical frequency f_{criti} still applies beyond which there is 10-fold relationship between normalized variance and time constant τ. For frequency close to DC, the normalized variance is large when the input signal amplitude is large, which may be due to the contribution of under-attenuated sum frequency signal as shown in Fig. 2(b). The effect of sum frequency can also be eliminated by choosing modulation frequency f_0 larger than critical frequency f_{criti}.

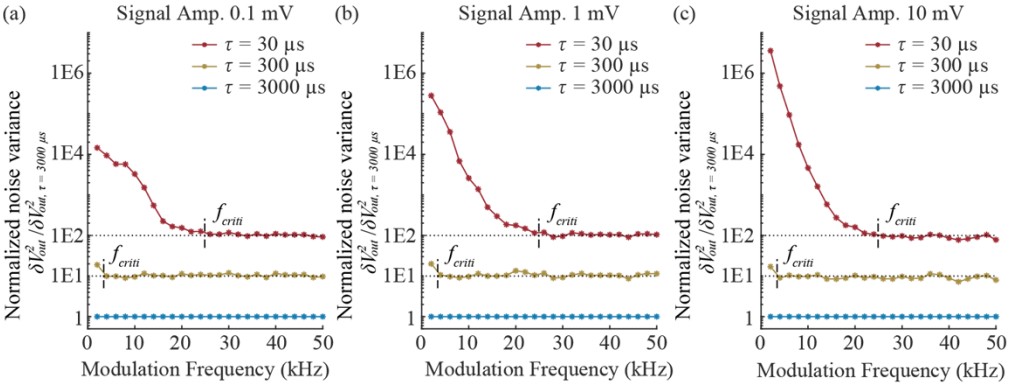

Fig. 4. Normalized noise variance with signal amplitude of (a) 0.1 mV, (b) 1 mV and (c) 10 mV

Biomedical Optics EXPRESS

Table 1 shows that before optimization ~ 74% of the OI-RD detection time is the wait time for LIA when the time constant τ is 300 µs and wait time is 3 ms. To minimize wait time in order to increase detection speed, small time constant τ and small LPF slope are desirable. However, time constant τ of 10 µs is too small to provide critical frequency f_{criti} smaller than modulation frequency f_0 which is fixed at 50 kHz for OI-RD microscope. Table 1 highlights those critical frequencies f_{criti} which are smaller than the modulation frequency f_0, among them time constant $\tau = 30$ µs and LPF slope of 24 dB/oct were chosen for further optimization since they may provide faster detection speed with lower noise level.

3.2. Performance of the first-generation amplifier

Decreasing time constant τ not only increases OI-RD detection speed but also may introduce more noises into OI-RD signals. Figure 5(a) shows OI-RD time series signals measured by first-generation amplifier with time constant τ changing from 3000 µs to 30 µs at a slope of 24 dB/oct. Clearly, variations of OI-RD signals become larger with decreasing time constant τ. Figure 5(b) shows the standard deviations of OI-RD time series signals normalized by OI-RD maximum signal [27], which are 1.72×10^{-4}, 5.43×10^{-4}, and 3.36×10^{-3} at time constant τ of 3000 µs, 300 µs and 30 µs, respectively. Figure 5(a) also shows the ground noise of first-generation amplifier which was measured by connecting the electronic amplifier to LIA without no light incident on the amplifier. The normalized standard deviations of first-generation amplifier ground noises are 1.10×10^{-4}, 3.77×10^{-4}, and 1.15×10^{-3} at time constant τ of 3000 µs, 300 µs and 30 µs, respectively.

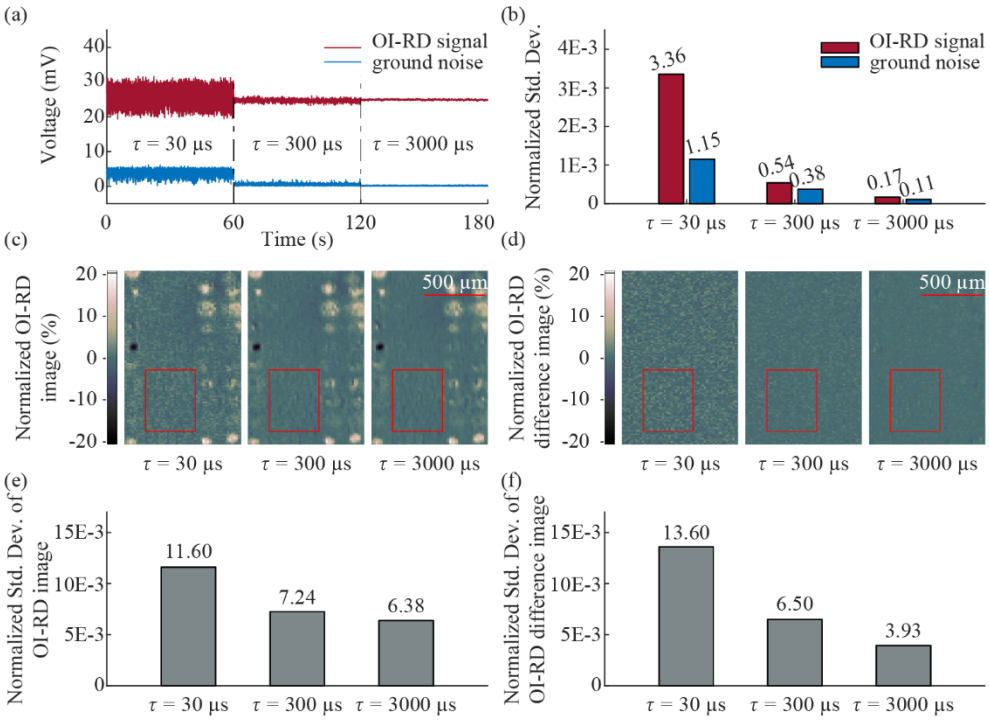

Fig. 5. Performance of the first-generation amplifier.

Figure 5(c) shows the normalized OI-RD images of microarray measured with time constant τ of 3000 µs, 300 µs and 30 µs. Figure 5(e) shows the normalized standard deviation of OI-RD image inside the area highlighted by red rectangle in Fig. 5(c). The normalized standard deviation

Biomedical Optics EXPRESS

of OI-RD image measured with time constant τ of 3000 µs is 6.38×10^{-3}, close to that measured with time constant τ of 300 µs, which is smaller than that measured with time constant τ of 30 µs.

For high-throughput screening, difference image of OI-RD image before reaction with protein from OI-RD image after reaction with protein is used to look for compounds binding to protein. It is thus important to characterize the normalized standard deviation of OI-RD difference images. Figure 5(d) shows that OI-RD difference images become smoother with increasing time constant τ and Fig. 5(f) shows that the normalized standard deviations of difference images (highlighted by red rectangle in Fig. 5(d)) are 3.93×10^{-3}, 6.50×10^{-3}, and 1.36×10^{-2} at time constant τ of 3000 µs, 300 µs and 30 µs, respectively.

To increase OI-RD detection speed, time constant τ was determined to decrease from 300 µs to 30 µs. Figure 5 demonstrates that the normalized standard deviations of OI-RD time series signals and images become larger with time constant τ decreasing to 30 µs measured by first-generation amplifier. Especially, the normalized standard deviation of time series OI-RD signal with time constant τ of 30 µs is 3.36×10^{-3} which is too large for screening applications. A second-generation amplifier is then designed to decrease the normalized standard deviation of time series OI-RD signal with time constant τ of 30 µs to 5.43×10^{-4}, close to the value measured by first-generation amplifier with time constant τ of 300 µs, which has been used for HTS screening all the time.

3.3. Development and performance of the second-generation amplifier

The normalized standard deviation of first-generation amplifier ground noise at time constant τ of 300 µs is 3.77×10^{-4}. When time constant τ decrease to 30 µs, the normalized standard deviation of ground noise increases up to 1.15×10^{-3}, which is already larger than the expected normalized standard deviation of OI-RD time series signal 5.43×10^{-4} for second-generation amplifier. It is thus important to develop second-generation amplifier with efforts to decrease both the amplifier ground noise and the OI-RD signal noise.

The first-generation amplifier comprised a transimpedance amplifier that converted current to voltage and a second stage amplifier (Fig. S3(a) within the Supplement 1). To minimize amplifier noise, a band-pass filter with a frequency range of 30 kHz to 120 kHz was integrated into the second-generation amplifier (Fig. S3(b) within the Supplement 1) to suppress noise outside of this range. Additionally, the second-generation amplifier includes several process improvements, including the use of solid-state aluminum polymer capacitors, tantalum capacitors, metal film resistors, and immersion gold circuit boards, all of which contribute to enhancing the performance and reliability of the amplifier.

The laser power incident upon the second-generation amplifier is constrained to a range of approximately 0.3 µW to 3 µW. Variations or instability in the laser power can cause extraneous noise to the OI-RD signal. Therefore, a highly stable laser is used to minimize such noise. The normalized standard deviation of the laser power is $\sim 1.97 \times 10^{-4}$, which is below the anticipated normalized standard deviation of $\sim 5.4 \times 10^{-4}$, indicating that the laser stability is sufficient for conducting OI-RD experiments.

With second-generation amplifier, the normalized standard deviation of OI-RD time series signal increases from 1.59×10^{-4} to 4.31×10^{-4} with time constant τ decreasing from 3000 µs to 30 µs, as shown in Fig. 6(a) and 6(b). Clearly, the normalized standard deviation of OI-RD time series signal measured by second-generation amplifier at time constant τ of 30 µs is 4.31×10^{-4}, which is smaller than the normalized standard deviation of 5.43×10^{-4} measured by first-generation amplifier at time constant τ of 300 µs, indicating that second-generation amplifier is indeed able to enable OI-RD to scan quickly without increasing noise level.

Figure 6(c) shows the normalized OI-RD images measured with time constant τ of 3000 µs, 300 µs and 30 µs and Fig. 6(e) shows the normalized standard deviations of OI-RD images inside the area highlighted by red rectangle in Fig. 6(c). The normalized standard deviations

Biomedical Optics EXPRESS

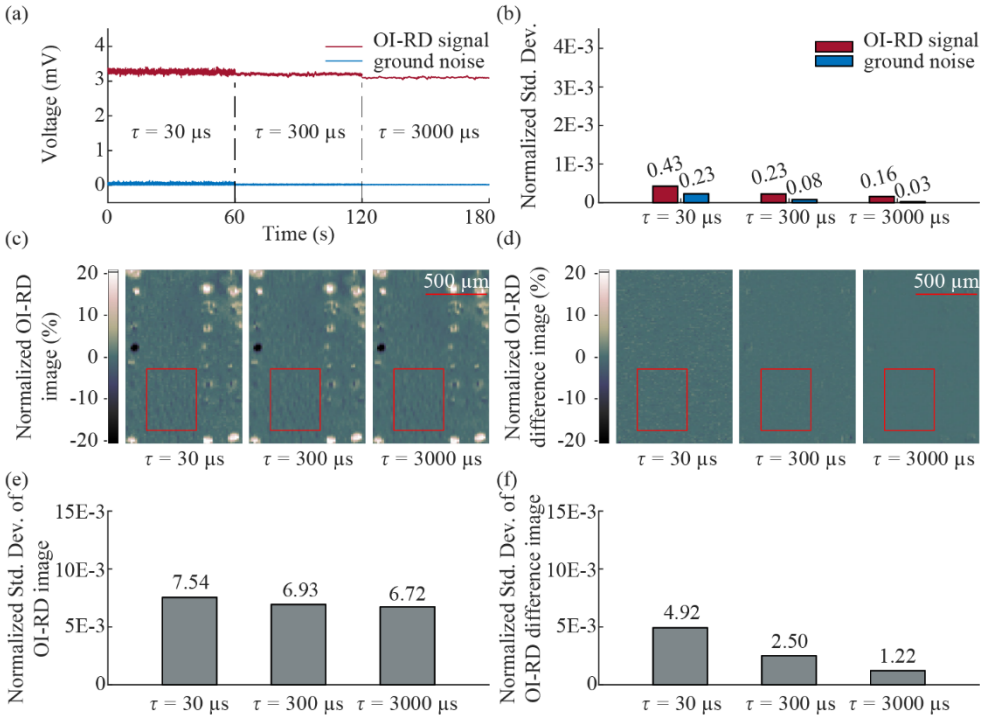

Fig. 6. Performance of the second-generation amplifier.

are 6.72×10^{-3}, 6.93×10^{-3}, and 7.54×10^{-3} with time constant τ of 3000 μs, 300 μs and 30 μs, which are close to values measured by first-generation amplifier with time constant τ of 3000 μs and 300 μs, demonstrating the normalized standard deviation about 7×10^{-3} is due to the signal difference causing by nonuniformity of substrate. The large normalized standard deviation measured by first-generation amplifier with time constant τ of 30 μs may be caused by large ground noise of first-generation amplifier.

Figure 6(d) shows the normalized difference images whose normalized standard deviations are shown in Fig. 6(f). OI-RD difference images are slightly smoother with increasing time constant and the normalized standard deviation of difference images (highlighted by red rectangle in Fig. 6(d)) are 1.22×10^{-3}, 2.50×10^{-3}, and 4.92×10^{-3} at time constant τ of 3000 μs, 300 μs and 30 μs, respectively. Again, the normalized standard deviation measured by second-generation amplifier at time constant τ of 30 μs is smaller than that measured by first-generation amplifier at time constant τ of 300 μs, demonstrating that second-generation amplifier is capable of increasing OI-RD detection speed without increasing noise.

By using time constant τ of 30 μs and LPF slope of 24 dB/oct, wait time between two OI-RD pixel data can be decreased to 0.3 ms, which decreases the total wait time for LIA of an OI-RD image from ~ 77 min (Table 1) to ~ 8 min. The detection speed of OI-RD microscope is thus greatly increased by selecting proper time constant τ and developing second-generation amplifier with the normalized standard deviation of OI-RD time series signal being 4.31×10^{-4}, which is similar to the value before speed optimization for OI-RD microscope.

3.4. *Minimization of the time required for software and translation stage movement*

After decrease of the wait time for LIA from ~ 77 min to ~ 8 min, ~ 20 min of acquiring data by software should be minimized for further OI-RD speed optimization. The software of OI-RD

Biomedical Optics EXPRESS

microscope includes a double loop structure as shown in Fig. 1(b), in which the inner loop calls the DAQmx Read VI for data acquisition. The DAQmx Read AI starts the acquisition task and stop the task once the last sample is acquired. Since DAQmx Read AI is used in a loop (Fig. 1(b)), the measurement starts and stops in each iteration, which significantly reduces the performance of the data acquisition. Explicitly staring the task prior to the loop (Fig. S4 within the Supplement 1) and stopping the task after the execution of the loop (Fig. S5 within the Supplement 1) significantly improves data acquisition performance. This change reduced the time consumption per pixel from ~ 780 µs to ~ 148 µs, resulting in a total data acquisition time reduction from around 20 min to about 4 min.

The last one for OI-RD speed optimization is the time for translation stage movement which was ~ 7 min, including the time before the translation stage movement t_b, and the time after translation stage movement t_a. This process is illustrated by the outer loop in Fig. 1(b).

To minimize t_b and t_a without affecting OI-RD image quality, 15 OI-RD images were obtained, with first 13 images having t_b of 0 ms and t_a of 0, 5, 10, 15, 20, 25, 30, 35, 40, 45, 50, 100, 150 ms, respectively. The remaining two images were obtained under identical conditions with t_b at 50 ms and t_a at 150 ms, which are parameters usually used to obtain OI-RD image before speed optimization. 14 difference images were obtained by subtracting images with different t_b and t_a from the last image with t_b of 50 ms and t_a of 150 ms, four of which are shown in Fig. 7(a). Clearly, decreasing t_a from 150 ms to 0 ms leads to more features appearing on the left side of the difference image so that the standard deviation of the left side (marked by a red rectangle) is measured. Figure 7(b) shows the relative standard deviation which is calculated by the standard deviation of difference images (subtracting image with $t_b = 50$ ms and $t_a = 150$ ms from images with $t_b = 0$ ms and $t_a = 0 \sim 150$ ms) being divided by that of difference image of two consecutive images with same t_b at 50 ms and t_a at 150 ms. The relative standard deviation is very large with t_a of 0, 5, and 10 ms, indicating that the left side of OI-RD image deviates a lot from that with t_b of 50 ms and t_a of 150 ms. The relative standard deviation decreases gradually with increasing t_a from 10 ms to 30 ms, then reaches a roughly constant level with t_a larger than 30 ms, demonstrating that the left side of OI-RD image gradually becomes similar to the image with t_b of 50 ms and t_a of 150 ms with increasing t_a. In addition, the last point in Fig. 7(b) is the relative standard deviation of difference image (subtracting image with $t_b = 50$ ms and $t_a = 150$ ms from image with $t_b = 0$ ms and $t_a = 150$ ms) whose value is 1.01, suggesting that t_b can be set to be 0 without affecting image quality.

Above results suggest that t_b of 0 ms and t_a of 30 ms could be used for speed optimization of OI-RD microscope without affecting image quality. With these values, the total time for translation stage movement decreases from ~ 7 min to ~ 1 minute.

3.5. OI-RD images before and after speed optimization

With a series of optimization methods, the time to scan an OI-RD image was significantly reduced. Specifically, the total wait time for LIA was decreased from ~ 77 min to ~ 8 min by proper selection of time constant τ and development of the second-generation amplifier. Optimization for the software and the translation stage reduced the time from ~27 min to ~ 4 min. After optimization, the time for an OI-RD image of a large microarray (1980 × 780 pixels) decreases from ~ 104 min to ~ 12 min and the detection speed is greatly increased. Figure 8 shows two OI-RD images obtained by first-generation amplifier at time constant τ of 300 µs (the middle one) and by second-generation amplifier at time constant τ of 30 µs (the right one) and the normalized standard deviations of both images are $\sim 7.24 \times 10^{-3}$ and $\sim 7.54 \times 10^{-3}$, respectively, which are smaller than that ($\sim 1.16 \times 10^{-2}$) of the image obtained by first-generation amplifier at time constant τ of 30 µs (the left one).

Biomedical Optics EXPRESS

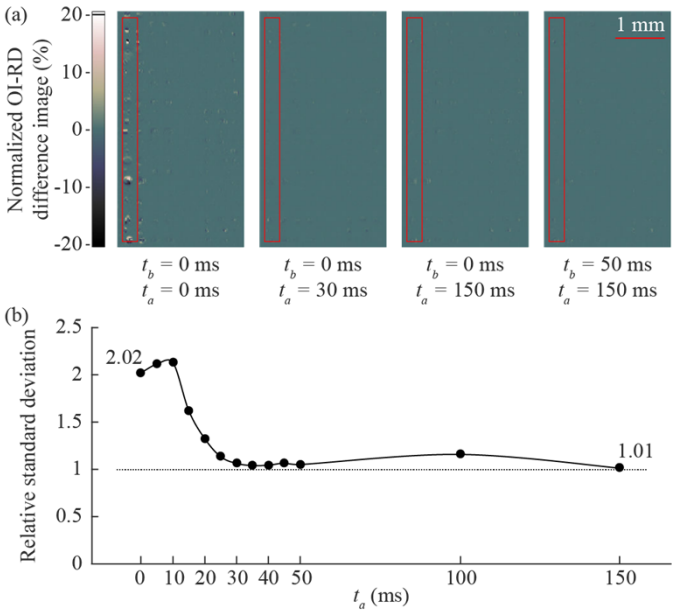

Fig. 7. (a) Normalized OI-RD difference images and (b) relative standard deviation of OI-RD difference images.

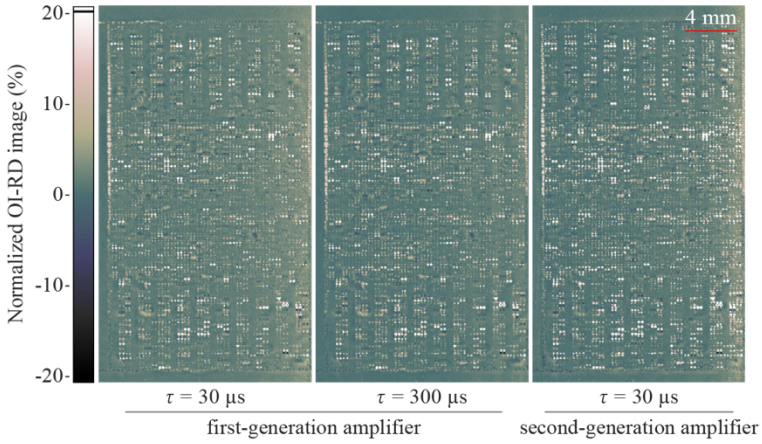

Fig. 8. OI-RD images obtained by first-generation amplifier and second-generation amplifier.

4. Conclusion

In conclusion, this work has optimized the performance of OI-RD microscope by decreasing the time required for scanning an OI-RD image from approximately 104 min to 12 min without affecting OI-RD image quality. As a result, the screening throughput of OI-RD microscope is expected to increase by an order of magnitude, from 20,000 samples per day to 200,000 samples per day, meeting the standards for uHTS, which may find more applications in the field of drug screening.

Funding. National Natural Science Foundation of China (32271510); Shanghai Natural Science Foundation (20ZR1403700, 20ZR1405100); Science and Technology Commission of Shanghai Municipality (20JC1410900);

Biomedical Optics EXPRESS

National Natural Science Foundation of China (82030106, 62175036, 62175034); National Key Research and Development Program of China (2021YFA0805200, 2021YFF0502900); Science and Technology Research Program of Shanghai (19DZ2282100); Shanghai Key Discipline Construction Plan (GWV-10.1-XK01); Shanghai Engineering Technology Research Center of Hair Medicine (19DZ2250500); Medical Engineering Fund of Fudan University (yg2021-022); Pioneering Project of Academy for Engineering and Technology, Fudan University (gyy2018-001, 002).

Disclosures. The authors declare no conflicts of interest.

Data availability. Data underlying the results presented in this paper are not publicly available at this time but may be obtained from the authors upon reasonable request.

Supplemental document. See Supplement 1 for supporting content.

References

1. V. Blay, B. Tolani, S. P. Ho, and M. R. Arkin, "High-Throughput Screening: today's biochemical and cell-based approaches," Drug Discov Today **25**(10), 1807–1821 (2020).
2. A. Carnero, "High throughput screening in drug discovery," Clin Transl Oncol **8**(7), 482–490 (2006).
3. N. Berdigaliyev and M. Aljofan, "An overview of drug discovery and development," Future Med Chem **12**(10), 939–947 (2020).
4. S. A. Sundberg, "High-throughput and ultra-high-throughput screening: solution- and cell-based approaches," Curr Opin Biotechnol **11**(1), 47–53 (2000).
5. A. Uri and O. E. Nonga, "What is the current value of fluorescence polarization assays in small molecule screening?" Expert Opin Drug Discov **15**(2), 131–133 (2020).
6. M. H. Roehrl, S. Kang, J. Aramburu, G. Wagner, A. Rao, and P. G. Hogan, "Selective inhibition of calcineurin-NFAT signaling by blocking protein-protein interaction with small organic molecules," Proc Natl Acad Sci U S A **101**(20), 7554–7559 (2004).
7. C. H. Kenny, W. Ding, K. Kelleher, S. Benard, E. G. Dushin, A. G. Sutherland, L. Mosyak, R. Kriz, and G. Ellestad, "Development of a fluorescence polarization assay to screen for inhibitors of the FtsZ/ZipA interaction," Anal Biochem **323**(2), 224–233 (2003).
8. X. Ye, R. Zhang, F. Lian, W. Zhang, W. Lu, J. Han, N. Zhang, J. Jin, C. Luo, K. Chen, F. Ye, and H. Ding, "The identification of novel small-molecule inhibitors targeting WDR5-MLL1 interaction through fluorescence polarization based high-throughput screening," Bioorg Med Chem Lett **29**(4), 638–645 (2019).
9. M. R. Zhu, D. H. Du, J. C. Hu, L. C. Li, J. Q. Liu, H. Ding, X. Q. Kong, H. L. Jiang, K. X. Chen, and C. Luo, "Development of a high-throughput fluorescence polarization assay for the discovery of EZH2-EED interaction inhibitors," Acta Pharmacol Sin **39**(2), 302–310 (2018).
10. Z. Li, S. Mehdi, I. Patel, J. Kawooya, M. Judkins, W. Zhang, K. Diener, A. Lozada, and D. Dunnington, "An ultra-high throughput screening approach for an adenine transferase using fluorescence polarization," J Biomol Screen **5**(1), 31–37 (2000).
11. C. McWhirter, M. Tonge, H. Plant, I. Hardern, W. Nissink, and S. T. Durant, "Development of a high-throughput fluorescence polarization DNA cleavage assay for the identification of FEN1 inhibitors," J Biomol Screen **18**(5), 567–575 (2013).
12. P. Guhathakurta, E. Prochniewicz, B. D. Grant, K. C. Peterson, and D. D. Thomas, "High-throughput screen, using time-resolved FRET, yields actin-binding compounds that modulate actin-myosin structure and function," J Biol Chem **293**(31), 12288–12298 (2018).
13. J. M. Rectenwald, P. B. Hardy, J. L. Norris-Drouin, S. H. Cholensky, L. I. James, S. V. Frye, and K. H. Pearce, "A general TR-FRET assay platform for high-throughput screening and characterizing inhibitors of methyl-lysine reader proteins," SLAS Discovery: Advancing Life Sciences R&D **24**, 693–700 (2019).
14. Y. Du, R. W. Fu, B. Lou, J. Zhao, M. Qui, F. R. Khuri, and H. Fu, "A time-resolved fluorescence resonance energy transfer assay for high-throughput screening of 14-3-3 protein-protein interaction inhibitors," Assay Drug Dev Technol **11**(6), 367–381 (2013).
15. J. Xiong, V. G. Pecchi, M. Qui, A. A. Ivanov, X. Mo, Q. Niu, X. Chen, H. Fu, and Y. Du, "Development of a Time-Resolved Fluorescence Resonance Energy Transfer Ultrahigh-Throughput Screening Assay for Targeting the NSD3 and MYC Interaction," Assay Drug Dev Technol **16**(2), 96–106 (2018).
16. A. Mazars and R. Fahraeus, "Using BRET to study chemical compound-induced disruptions of the p53-HDM2 interactions in live cells," Biotechnol J **5**(4), 377–384 (2010).
17. I. Weibrecht, K. J. Leuchowius, C. M. Clausson, T. Conze, M. Jarvius, W. M. Howell, M. Kamali-Moghaddam, and O. Soderberg, "Proximity ligation assays: a recent addition to the proteomics toolbox," Expert Rev Proteomics **7**(3), 401–409 (2010).
18. G. Zimmermann, B. Papke, S. Ismail, N. Vartak, A. Chandra, M. Hoffmann, S. A. Hahn, G. Triola, A. Wittinghofer, P. I. Bastiaens, and H. Waldmann, "Small molecule inhibition of the KRAS-PDEdelta interaction impairs oncogenic KRAS signalling," Nature **497**(7451), 638–642 (2013).
19. K. Stegmaier, J. S. Wong, K. N. Ross, K. T. Chow, D. Peck, R. D. Wright, S. L. Lessnick, A. L. Kung, and T. R. Golub, "Signature-based small molecule screening identifies cytosine arabinoside as an EWS/FLI modulator in Ewing sarcoma," PLoS Med **4**(4), e122 (2007).

Biomedical Optics EXPRESS

20. A. J. Vegas, J. E. Bradner, W. Tang, O. M. McPherson, E. F. Greenberg, A. N. Koehler, and S. L. Schreiber, "Fluorous-based small-molecule microarrays for the discovery of histone deacetylase inhibitors," Angew Chem Int Ed Engl **46**(42), 7960–7964 (2007).
21. H. Miao, J. A. Tallarico, H. Hayakawa, K. Munger, J. L. Duffner, A. N. Koehler, S. L. Schreiber, and T. A. Lewis, "Ring-opening and ring-closing reactions of a shikimic acid-derived substrate leading to diverse small molecules," J Comb Chem **9**(2), 245–253 (2007).
22. Y. Fei, Y. S. Sun, Y. Li, K. Lau, H. Yu, H. A. Chokhawala, S. Huang, J. P. Landry, X. Chen, and X. Zhu, "Fluorescent labeling agents change binding profiles of glycan-binding proteins," Mol Biosyst **7**(12), 3343–3352 (2011).
23. Y. S. Sun, "Use of Microarrays as a High-Throughput Platform for Label-Free Biosensing," J Lab Autom **20**(4), 334–353 (2015).
24. X. Zhu, J. P. Landry, Y. S. Sun, J. P. Gregg, K. S. Lam, and X. Guo, "Oblique-incidence reflectivity difference microscope for label-free high-throughput detection of biochemical reactions in a microarray format," Appl. Opt. **46**(10), 1890–1895 (2007).
25. Y. Y. Fei, J. P. Landry, Y. S. Sun, X. D. Zhu, J. T. Luo, X. B. Wang, and K. S. Lam, "A novel high-throughput scanning microscope for label-free detection of protein and small-molecule chemical microarrays," Rev. Sci. Instrum. **79**(1), 013708 (2008).
26. C. Zhu, X. Zhu, J. P. Landry, Z. Cui, Q. Li, Y. Dang, L. Mi, F. Zheng, and Y. Fei, "Developing an Efficient and General Strategy for Immobilization of Small Molecules onto Microarrays Using Isocyanate Chemistry," Sensors **16**(3), 378 (2016).
27. C. Zhu, R. Chen, Y. Zhu, X. Wang, X. Zhu, L. Mi, F. Zheng, and Y. Fei, "Calibration of oblique-incidence reflectivity difference for label-free detection of a molecular layer," Appl. Opt. **55**(33), 9459–9466 (2016).
28. Y. Ding, D. Xing, Y. Fei, and B. Lu, "Emerging degrader technologies engaging lysosomal pathways," Chem Soc Rev **51**(21), 8832–8876 (2022).
29. Z. Li, C. Wang, and Z. Wang, *et al.*, "Allele-selective lowering of mutant HTT protein by HTT-LC3 linker compounds," Nature **575**(7781), 203–209 (2019).
30. J. P. Landry, Y. Fei, and X. D. Zhu, "High Throughput, Label-free Screening Small Molecule Compound Libraries for Protein-Ligands using Combination of Small Molecule Microarrays and a Special Ellipsometry-based Optical Scanner," Int Drug Discov, 8–13 (2011).
31. J. P. Landry, Y. Fei, X. Zhu, Y. Ke, G. Yu, and P. Lee, "Discovering small molecule ligands of vascular endothelial growth factor that block VEGF-KDR binding using label-free microarray-based assays," Assay Drug Dev Technol **11**(5), 326–332 (2013).
32. J. Wang, C. Zhu, D. Song, R. Xia, W. Yu, Y. Dang, Y. Fei, L. Yu, and J. Wu, "Epigallocatechin-3-gallate enhances ER stress-induced cancer cell apoptosis by directly targeting PARP16 activity," Cell Death Discov **3**(1), 17034 (2017).
33. H. Song, C. Wang, C. Zhu, Z. Wang, H. Yang, P. Wu, X. Cui, J. Botas, Y. Dang, Y. Ding, Y. Fei, and B. Lu, "Suppression of toxicity of the mutant huntingtin protein by its interacting compound, desonide," Proc Natl Acad Sci U S A **119**(10), e2114303119 (2022).
34. J. Gao, M. Zheng, and X. Wu, *et al.*, "CDK inhibitor Palbociclib targets STING to alleviate autoinflammation," EMBO Rep **23**(6), e53932 (2022).
35. K. Libbrecht, E. Black, and C. Hirata, "A basic lock-in amplifier experiment for the undergraduate laboratory," Am. J. Phys. **71**(11), 1208–1213 (2003).
36. S. DeVore, A. Gauthier, J. Levy, and C. Singh, "Development and evaluation of a tutorial to improve students' understanding of a lock-in amplifier," Phys. Rev. Phys. Educ. Res. **12**(2), 020127 (2016).
37. F. N. Hooge, "1/f noise sources," IEEE Trans. Electron Devices **41**(11), 1926–1935 (1994).
38. E. Milotti, "1/f noise: a pedagogical review," arXiv, physics/0204033 (2002).
39. D. A. Van Baak and G. Herold, "Response of a lock-in amplifier to noise," Am. J. Phys. **82**(8), 785–797 (2014).